

# Blocking, descent and gravity waves: Observations and modelling of a MAP northerly föhn event

By QINGFANG JIANG<sup>1\*</sup>, JAMES D. DOYLE<sup>2</sup> and RONALD B. SMITH<sup>3</sup>

<sup>1</sup>University Corporation for Atmospheric Research, Monterey, USA

<sup>2</sup>Naval Research Laboratory, Monterey, USA

<sup>3</sup>Yale University, New Haven, USA

(Received 8 September 2003; revised 10 August 2004)

## SUMMARY

A northerly föhn event observed during the special observational period of the Mesoscale Alpine Programme is investigated based on observational analysis and numerical modelling. The focus of this study includes three dynamical processes associated with mountain perturbations and their interactions, namely, windward flow blocking, descent and warming on the lee side, and mountain waves. Observations indicate the presence of a deep weak-flow layer underneath a stable layer, associated with Alpine-scale blocking. Satellite imagery reveals a föhn-induced cloud-free area to the south of the Alps, which is consistent with flow descent diagnosed from radiosondes and constant-volume balloons. Moderate-amplitude stationary waves were observed by research aircraft over the major Alpine peaks. Satellite images and balloon data indicate the presence of stationary trapped-wave patterns located to the north of the Alpine massif.

Satisfactory agreement is found between observations and a real-data COAMPS simulation nested to 1 km resolution. COAMPS indicates the presence of trapped waves associated with a sharp decrease of Scorer parameter above a stable layer in the mid-troposphere. Underneath the stable layer, moist low-level flow is blocked to the north of the Alps. The warm air in the stable layer descends in the lee and recovers its altitude over a relatively short horizontal distance through a hydraulic jump.

Blocking reduces the effective mountain and hence significantly reduces mountain drag. A simple empirical formula for estimation of the effective mountain height,  $h_e$ , is derived based on numerical simulations. The formula states  $h_e/h_c = \sqrt{h/h_c}$ , where  $h$  is the real mountain height and  $h_c$  is the critical mountain height to have flow stagnation.

KEYWORDS: Evanescent wave Hydraulic jump Mountain drag

## 1. INTRODUCTION

Perturbations introduced by mesoscale terrain can be coarsely classified into four categories: windward blocking, lee-side flow descent associated with the development of severe downslope winds, gravity waves, and potential vorticity (PV) generation associated with dissipative processes such as wave breaking. If the mountain is high enough, as measured by a non-dimensional mountain height,  $M (= Nh_m/U$  where  $N$  is buoyancy frequency,  $h_m$  is mountain height, and  $U$  is the ambient cross-mountain wind speed), flow stagnation appears over the windward slope associated with either flow splitting or flow reversal. According to previous studies, the critical non-dimensional mountain height,  $M_c$ , to have windward stagnation varies with mountain shape and aspect ratio (Smith 1989), ranging from 0.85 for a two-dimensional (2D) ridge (Huppert and Miles 1969) to 1.32 for 3D circular terrain (Jiang 2003). For barriers with large horizontal dimensions, the influence of the earth's rotation for blocking effects has been investigated by Pierrehumbert and Wyman (1985) and Ólafsson and Bougeault (1997). Blocking and associated pressure drag have also been examined in case-studies (e.g. Hafner and Smith 1985; Chen and Smith 1987; Mayr and McKee 1995; Ólafsson and Bougeault 1997). The fundamentals of mountain-wave dynamics can be understood using linear wave theory (e.g. Queney 1948; Smith 1980) until wave breaking occurs which dissipates wave energy. In response to terrain forcing, low-level airflow tends to

\* Corresponding author: Naval Research Laboratory, 7 Grace Hopper Av., Monterey, CA 93943-5502, USA.  
e-mail: jiang@nrlmry.navy.mil

# Report Documentation Page

Form Approved  
OMB No. 0704-0188

Public reporting burden for the collection of information is estimated to average 1 hour per response, including the time for reviewing instructions, searching existing data sources, gathering and maintaining the data needed, and completing and reviewing the collection of information. Send comments regarding this burden estimate or any other aspect of this collection of information, including suggestions for reducing this burden, to Washington Headquarters Services, Directorate for Information Operations and Reports, 1215 Jefferson Davis Highway, Suite 1204, Arlington VA 22202-4302. Respondents should be aware that notwithstanding any other provision of law, no person shall be subject to a penalty for failing to comply with a collection of information if it does not display a currently valid OMB control number.

1. REPORT DATE <b>10 AUG 2004</b>		2. REPORT TYPE		3. DATES COVERED <b>00-00-2004 to 00-00-2004</b>	
4. TITLE AND SUBTITLE <b>Blocking, descent and gravity waves: Observations and modelling of a MAP northerly fohn event</b>				5a. CONTRACT NUMBER	
				5b. GRANT NUMBER	
				5c. PROGRAM ELEMENT NUMBER	
6. AUTHOR(S)				5d. PROJECT NUMBER	
				5e. TASK NUMBER	
				5f. WORK UNIT NUMBER	
7. PERFORMING ORGANIZATION NAME(S) AND ADDRESS(ES) <b>Naval Research Laboratory, 7 Grace Hopper Ave., Stop 2, Monterey, CA, 93943-5502</b>				8. PERFORMING ORGANIZATION REPORT NUMBER	
9. SPONSORING/MONITORING AGENCY NAME(S) AND ADDRESS(ES)				10. SPONSOR/MONITOR'S ACRONYM(S)	
				11. SPONSOR/MONITOR'S REPORT NUMBER(S)	
12. DISTRIBUTION/AVAILABILITY STATEMENT <b>Approved for public release; distribution unlimited</b>					
13. SUPPLEMENTARY NOTES					
14. ABSTRACT					
15. SUBJECT TERMS					
16. SECURITY CLASSIFICATION OF:			17. LIMITATION OF ABSTRACT	18. NUMBER OF PAGES	19a. NAME OF RESPONSIBLE PERSON
a. REPORT <b>unclassified</b>	b. ABSTRACT <b>unclassified</b>	c. THIS PAGE <b>unclassified</b>			

descend over the lee slope of mountain barriers, associated with the enhancement of surface wind (e.g. Klemp and Lilly 1975, Smith 1985, among many others).

While numerous idealized studies can be found in each category, examples based on well-documented observations are still rare. The objective of the Mesoscale Alpine Program (MAP) is to improve the understanding and modelling of mesoscale processes over complex terrain (Bougeault *et al.* 2001). On 8 November 1999, both the European Centre for Medium-range Weather Forecasts (ECMWF) and German/Swiss high-resolution models predicted strong northerly föhn across the Alps. Advanced Very High Resolution Radiometer (AVHRR) images indicated a spectacular föhn window located to the south of the Alps. Nested mesoscale models—the Canadian Mesoscale Compressible Community model (MC2,  $\Delta x = 3$  km) and the Naval Research Laboratory (NRL) Coupled Ocean–Atmospheric Mesoscale Prediction System (COAMPS,  $\Delta x = 4$  km)—predicted strong gravity-wave activity over the central Alpine massif and PV banners to the south of the Alps. Based on mesoscale model forecasts, five research aircraft were sent to fly coordinated missions across the central Alps and in the Po Valley to sample gravity waves and PV banners. Dozens of Global Positioning System (GPS) dropsondes were deployed during the flight.

The primary results from the gravity-wave flight are surprising. Despite the strong northerly wind across the Alps observed by radiosondes and the presence of the föhn window observed by satellites, only one of the aircraft, flying at relatively low levels (5.7 and 6 km), observed moderate waves with vertical speed  $w_{\max} = 6.1$  and  $5.8$  m s<sup>-1</sup> during two of its ten transverses. The maximum vertical motion sampled along other transverses or by other aircraft was less than 3 m s<sup>-1</sup>. Two hypotheses were proposed after the flight. One was that wave breaking occurred in the mid-troposphere, which decoupled the low-level flow with strong wave activity and downslope winds from the relatively quiescent flow above, such as described by Smith (1985). Therefore, the aircraft flying above the stagnant layer did not encounter any large-amplitude waves. The second hypothesis was that the waves were evanescent and decayed with altitude rapidly. The observations provide a comprehensive dataset for the study of dynamics associated with a northerly föhn over the Alps. This northerly föhn event has been examined by Smith (2004) with focus on model validation and Flamant *et al.* (2004) with focus on lee-side secondary PV banners. The goal of this study is to investigate the interactions among dynamical processes associated with mountain perturbations through the analysis of observational data and diagnosis of a COAMPS real-data simulation and two sensitivity simulations performed with half-terrain and quarter-terrain heights.

The remainder of this paper is organized as follows. Section 2 includes an overview of synoptic conditions and a description of research flight patterns and other observational platforms. The relevant observational data are analyzed in section 3. A comparison between a real-data COAMPS simulation and observations is given in section 4. Some dynamical aspects of this föhn event are discussed in section 5. The results are summarized in section 6.

## 2. SYNOPTIC OVERVIEW AND OBSERVATION DESCRIPTION

During MAP Intensive Observational Period (IOP) 15 (i.e. 6–8 November 1999), an anticyclone developed to the west of France and a cut-off low was located over Sicily, which resulted in relatively large pressure gradients across the Alps. Accordingly, a persistent deep northerly föhn swept over the entire Alps (Jiang *et al.* 2003; Flamant *et al.* 2004; Smith 2004). On the morning of 8 November, the cut-off low over Sicily was

slowly moving toward the south-east with a rainfall/snowfall region slowly retreating to the south. Over the eastern Alps, the surface pressure gradient was weakened by the development of another cut-off low over eastern Austria. The zonal wind gradient was evident at 500 hPa; the northerly wind reached  $35 \text{ m s}^{-1}$  over the eastern Alps and  $25 \text{ m s}^{-1}$  over the western Alps (Fig 1(a)).

The wind speed was much weaker at 850 hPa and low-level stagnant flow was evident immediately to the north of the central Alps (near  $9^{\circ}\text{E}$ ). To the east and west of the central Alps, the air tended to flow around the Alpine ridge, suggestive of flow splitting (Fig. 1(b)). Apparently, the presence of the cut-off low located to the north-east of the Alps increased the zonal pressure gradient and enhanced the northerly wind aloft. Near the surface, the cut-off low reduced the cross-Alpine pressure gradient, and therefore weakened the northerly wind. The low-level air to the north of the Alps was much more moist than that to the south. In summary, this northerly föhn event was characterized by strong northerly flow aloft and weaker flow near the ground. Windward blocking and lee-side descent were likely to occur.

From approximately 1000 to 1430 UTC on 8 November 1999, three research aircraft flew over the central Alps to sample gravity waves; the UK C-130 equipped with flight-level instruments and GPS dropsondes, the Deutsches Zentrum für Luft und Raumfahrt (DLR) Falcon equipped with flight-level instruments, downward-looking differential absorption lidar (DIAL) and GPS dropsondes, and the National Center for Atmospheric Research (NCAR) Electra equipped with flight-level instruments, downward-looking scanning aerosol backscatter lidar (SABL) and GPS dropsondes. Each of the three research aircraft flew a total of ten flight legs across the Alpine crest. The flight tracks were approximately oriented along the mean wind direction. The Electra flight segments are indicated by white lines on Fig. 2 with the terrain shaded. The segments were oriented approximately along four lines, which we refer to as the western track I (WT1), western track II (WT2), western track III (WT3), and eastern track (ET). WT1 and WT2 passed two ridge-like mountain ranges, the Berner Alpen and Alpi Pennine, and two major valleys, the Rhône and Aosta. The NCAR Electra executed two legs and the UK C-130 flew ten legs approximately along WT1, which passed peaks Jungfrau ( $46.5^{\circ}\text{N}$ ,  $8.0^{\circ}\text{E}$ ,  $4158 \text{ m}^*$ ) and Matterhorn ( $46.0^{\circ}\text{N}$ ,  $7.7^{\circ}\text{E}$ ,  $4478 \text{ m}$ ). The NCAR Electra executed two legs along WT2 which passed over the highest peak of Monte Rosa, Dufourspitze ( $4634 \text{ m}$ ), and the highest peak of the Berner Alpen, Finsteraarhorn ( $4274 \text{ m}$ ). The DLR Falcon flew six legs along WT1 and four legs along ET. The decision to shift from the western tracks to the eastern track was made by in-flight scientists in an attempt to measure larger-amplitude waves. In the early afternoon, two other research aircraft flew in the Po valley sampling secondary PV banners (Flamant *et al.* 2004).

### 3. OBSERVATIONS

#### (a) Satellite imagery

Two AVHRR visible images of the Alpine area are shown in Fig. 3 for 0718 and 1324 UTC on 8 November 1999. AVHRR is a broad-band, five-channel scanner and the ground resolution of its visible channel is approximately 1 km at nadir. Several interesting features can be seen from the AVHRR images. At 0718 UTC, the Alps are covered with thin altocumulus. A narrow föhn window is located to the south of the Alpine ridge, indicative of strong flow descent (Hoinka 1985). The föhn window separates large patches of altocumulus downstream from the Alpine massif. At 1324 UTC,

\* All altitudes are above mean sea level.

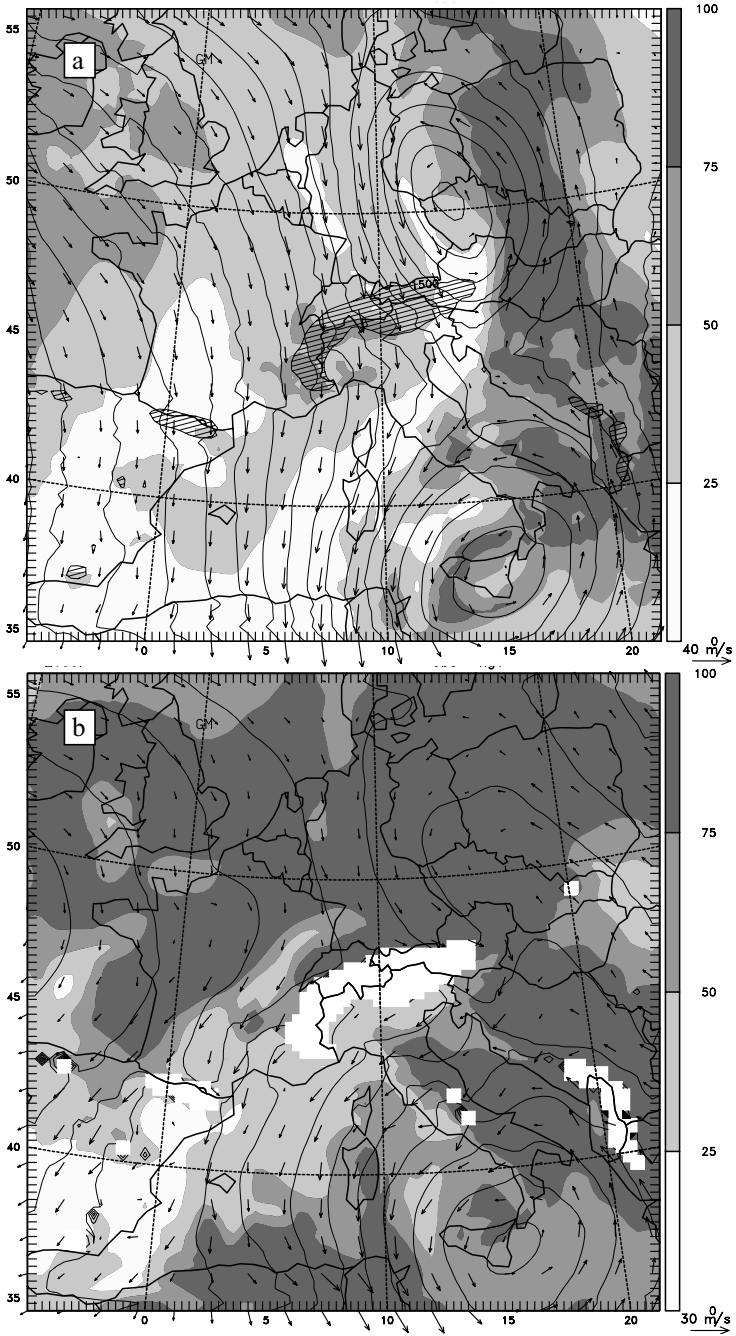


Figure 1. Geopotential height (contour interval = 20 gpm), wind vectors, and relative humidity (grey scale) at (a) 500 hPa and (b) 850 hPa, derived from COAMPS 27 km mesh valid at 1200 UTC on 8 November 1999.

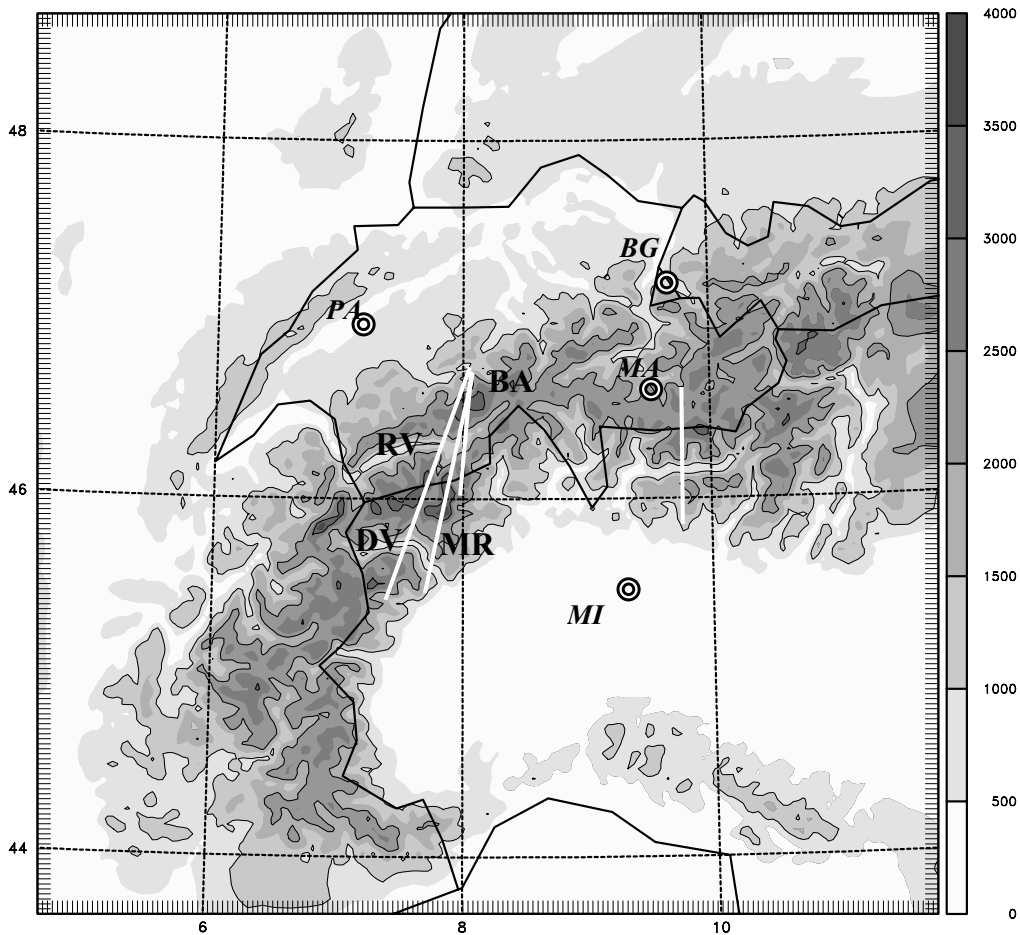


Figure 2. Topography (grey scale, m) of the central Alps with some geographic locations marked: Monte Rosa (MR), Berner Alpen (BA), Aosta valley (DV) and Rhone valley (RV). Radiosonde stations: Payerne (PA), Buchs-Grabs (BG), Masein (MA) and Milano (MI). NCAR Electra flight tracks are shown as white lines.

low clouds were mostly confined to the north side of the Alps. Quasi-2D wave clouds are evident between  $46^{\circ}$  and  $47^{\circ}$ N. In general, there are more wave clouds to the east of  $9^{\circ}$ E and fewer wave clouds to the west. Between  $46^{\circ}$  and  $47^{\circ}$ N, there are at least ten distinct waves along  $12^{\circ}$ E, corresponding to an approximate wavelength of 6–8 km.

A spectacular föhn window is located to the south of the Alps with arc-shaped clouds downstream, which is captured by the COAMPS real-data simulation (see relative humidity field in Fig. 1(b)). The south–north dimension of the föhn window is more than 200 km. According to COAMPS, the formation of the arc-shaped cloud is associated the advection of moist air by the Sicily cyclone.

During MAP IOPs, rapid scans of the Meteosat-6 geostationary satellite over the Alpine area were activated by EUMETSAT. Snapshots of the whole Alpine area were taken every 5 minutes over a period of 24 hours for each IOP. The horizontal resolution of rapid-scan imagery is relatively low (visible: 3–4 km). Animation of the rapid-scan imagery between 0800 and 1400 UTC reveals the southward advection of clouds to the north of the Alps, the expansion of the föhn window, and the presence of stationary

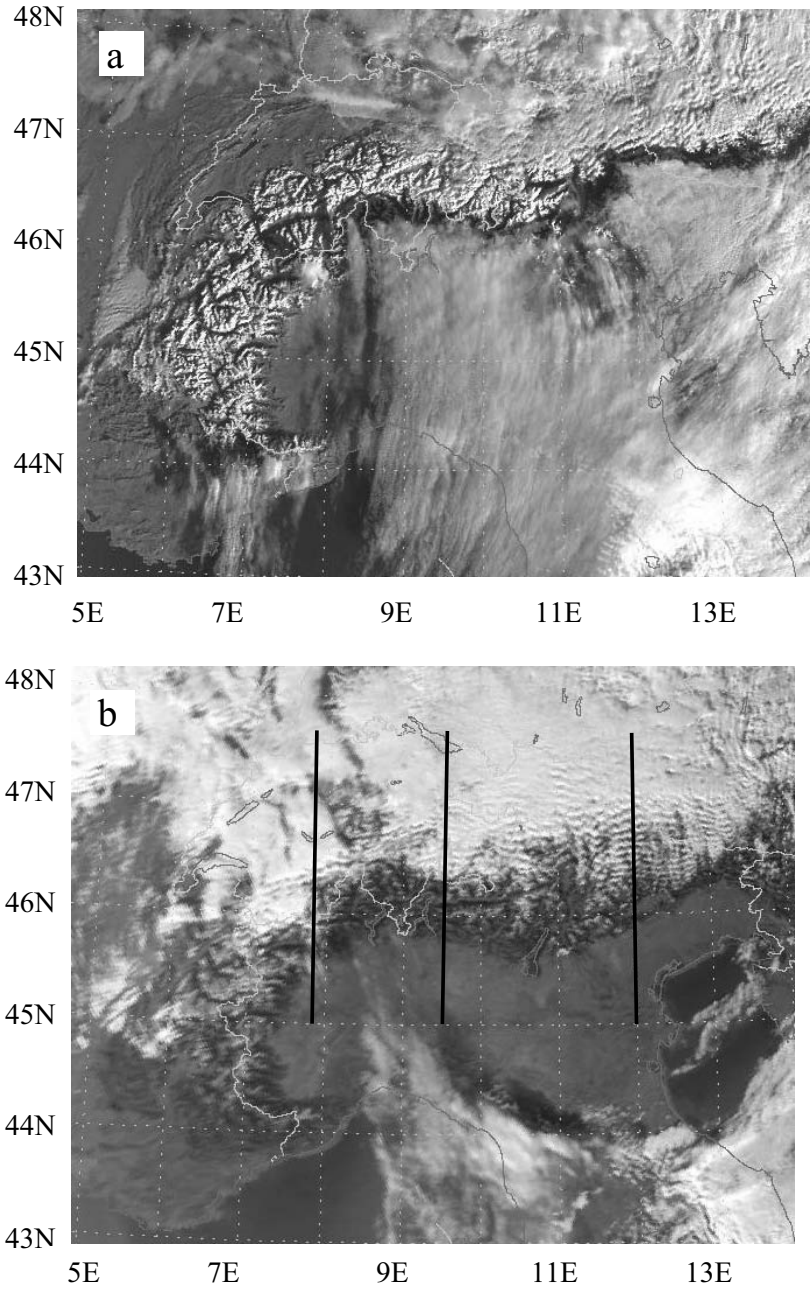


Figure 3. Visible AVHRR images taken at (a) 0718 UTC and (b) 1324 UTC on 8 November 1999. The three dark lines in (b) indicate the locations of the time–distance diagrams in Fig. 4.

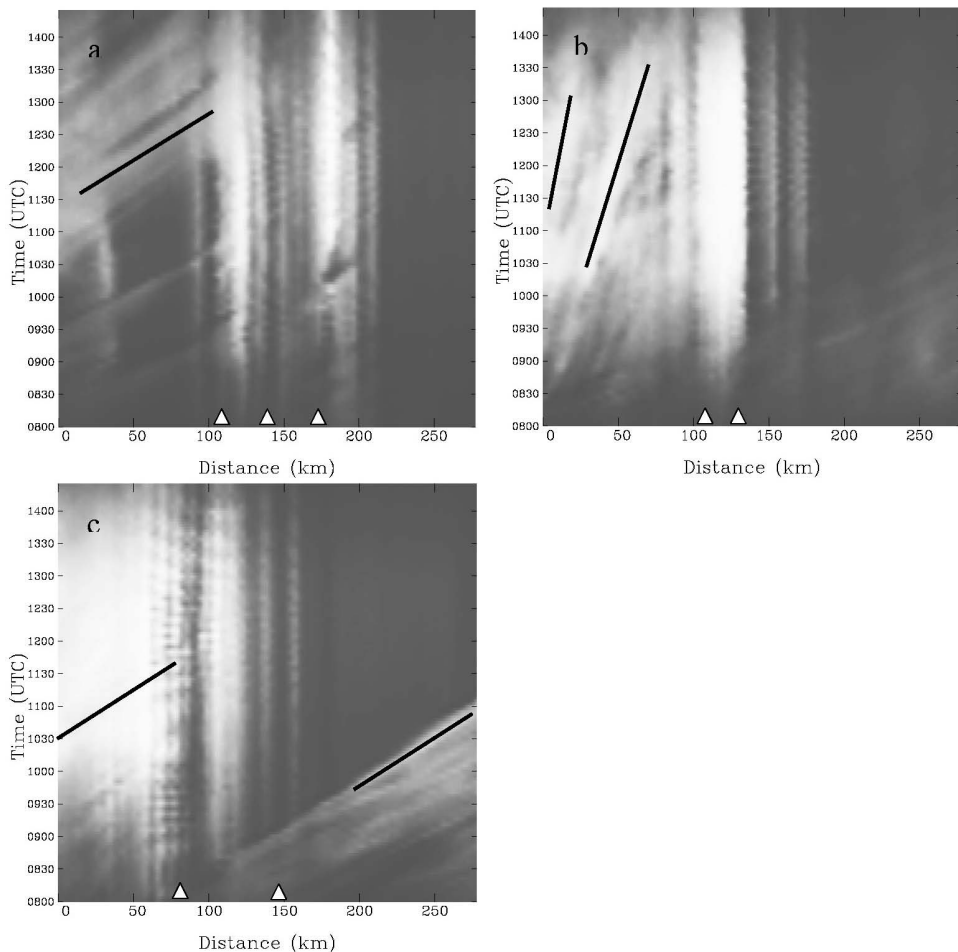


Figure 4. Hovmüller diagrams derived from Meteosat-6 rapid-scan digital data from 0800 to 1430 UTC on 8 November 1999 along the three lines shown in Fig. 3: (a)  $7.8^{\circ}\text{E}$ , (b)  $9.5^{\circ}\text{E}$  and (c)  $12^{\circ}\text{E}$ . Dark lines indicate some drifting features. Peaks above 2 km are indicated by white triangles.

bright/dark patterns over the Alpine region. We interpret these stationary patterns as alternating wave crests (clouds) and troughs (cloud-free).

To distinguish between the stationary and transitory features, time–distance (i.e. Hovmüller) diagrams are created along three north–south lines between  $45^{\circ}\text{N}$  and  $47.5^{\circ}\text{N}$  (see Fig. 3(b) for locations of these lines). The rapid-scan digital data have been processed to remove the temporal change in reflected radiance due to the rising sun and to improve the contrast. In these diagrams, drifting cloud elements appear as rightward (i.e. downstream) slanting bright features and stationary wave-cloud crests appear as vertically oriented bright features. The Hovmüller diagram along  $7.8^{\circ}\text{E}$  is shown in Fig. 4(a). Both propagating clouds upstream of  $46.5^{\circ}\text{N}$  and stationary wave clouds between  $45.5$  and  $46.5^{\circ}\text{N}$  are evident. Considering that the mean wind direction is approximately northerly, the advection speed of clouds can be estimated from the slopes of the drifting features. According to Fig. 4(a), the cloud advection speed is approximately  $20\text{ m s}^{-1}$ . Stationary (i.e. parallel to the time axis) bright patches are located in the lee of both Finsteraarhorn and Monte Rosa, and at

least three stationary wave crests are located between the two cloud patches and approximately over the Rhône valley. The cloud advection speed along 9.5°E longitude (i.e. approximately along the Electra eastern track) is much slower, approximately 3–5 m s<sup>-1</sup> (Fig. 4(b)). Several stationary wave crests to the north of the Alpine main massif are evident. Along 12°E (Fig. 4(c)) and to the north of 47°N, low-level clouds advect at 16 m s<sup>-1</sup>. Advective features are also evident to the south of the Alps, corresponding to the expansion of the föhn window. The cloud advection speed is approximately 18 m s<sup>-1</sup> at 12°E and the clouds retreat to the south of 45°N by 1100 UTC. Several stationary wave crests are evident between 46 and 47°N with a wavelength of approximately 7 km.

In general, due to the lower resolution of rapid-scan images, the waves are not as clearly discernible as in the AVHRR images. However, the high-frequency rapid-scan images clearly indicate the presence of stationary and persistent waves. The image analysis also raises some interesting questions regarding the dynamics associated with the observed features.

The advection of cumulus to the north of the Alps is apparently associated with synoptic-scale motion, which is probably modulated by the Alps. According to other observations (i.e. SABL), the clouds are located between 3 and 4 km. If we assume these clouds are advected at the wind speed of the cloud level, the along-Alps variation of the horizontal wind speed is striking. While the northerly wind is strong to the north of the eastern and western Alps, the wind is remarkably weak to the north of the central Alps (~9.5°E). Does this imply a 3 km (or deeper) nearly stagnant layer around the central Alps? If so, is it solely caused by Alpine blocking? Another question is related to the formation of the föhn window. Are the lee clouds shown in Fig. 3(a) associated with hydraulic jumps as identified by Jiang *et al.* (2003)? These issues will be further investigated using other observational data and the COAMPS real-data simulation.

### (b) Soundings

During MAP IOPs, the radiosonde network in the Alpine area was enhanced in both space and time. To examine large-scale aspects of flow across the Alps, several soundings are analysed in this section. Locations of the radiosonde stations of interest are shown in Fig. 2. Profiles of the  $v$  wind component, potential temperature, buoyancy frequency  $N$ , and Scorer parameter  $l$ , derived from two upstream 1200 UTC soundings, Payerne (46.8°N, 6.95°E, 490 m) and Buchs-Grab (47.18°N, 9.47°E, 445 m), are shown in Fig. 5. Payerne is located to the north-west of the western flight track (WT1) and Buchs-Grab is located approximately upstream of the eastern track. The Scorer parameter,  $l$ , is defined as (Scorer 1949)

$$l^2 = \frac{N^2}{U^2} - \frac{1}{U} \frac{\partial^2 U}{\partial z^2}. \quad (1)$$

Upstream of the western Alps, the layered structure of the stratification is evident. There is a relatively stable layer located between 1 and 3 km with an average buoyancy frequency  $N = 0.013 \text{ s}^{-1}$ .  $N$  is reduced to approximately  $0.01 \text{ s}^{-1}$  above and below the stable layer. At Payerne, the northerly wind component is relatively weak ( $< 10 \text{ m s}^{-1}$ ) below 3 km and the wind direction is north-easterly (not shown), probably associated with flow blocking by the main Alpine ridge. A widely used index for terrain-induced flow blocking is the non-dimensional mountain height  $M = Nh_m/U$ . The buoyancy stability  $N$  below 3 km is about  $0.013 \text{ s}^{-1}$  and the average cross-mountain wind speed

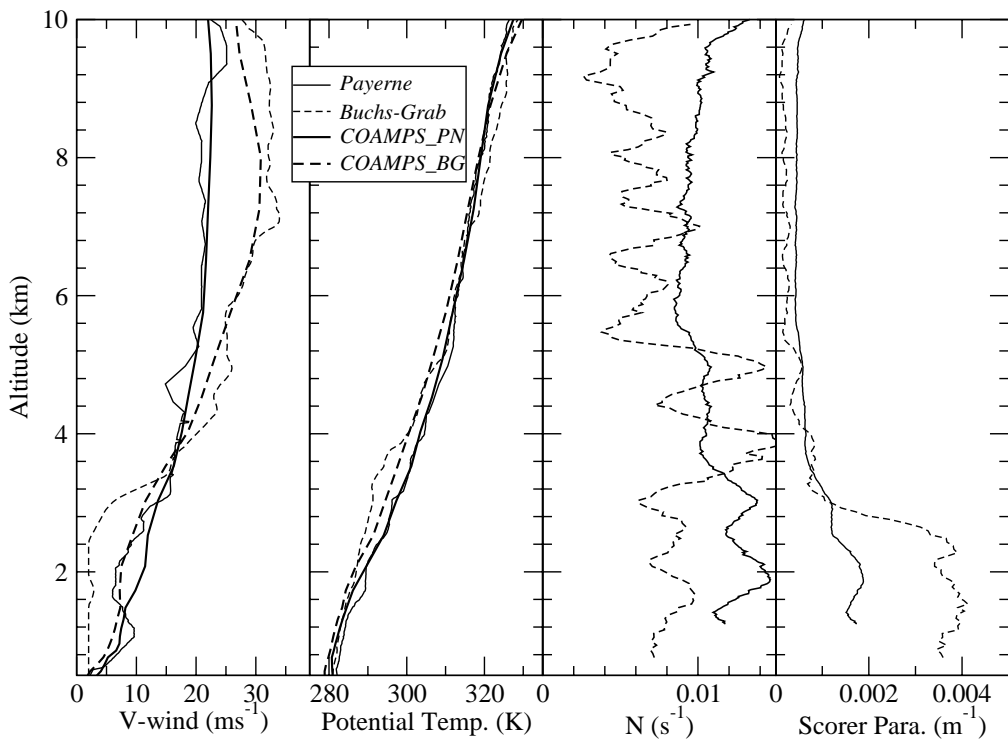


Figure 5. Profiles of meridional wind speed, potential temperature, static stability  $N$ , and Scorer parameter derived from the Payerne and Buchs-Grab soundings at 1200 UTC on 8 November 1999. The meridional wind speed and potential temperature profiles at nearest points on the COAMPS fourth grid mesh are plotted for comparison.

$U$  is approximately  $8 \text{ m s}^{-1}$ . If we use 3 km as the mountain height  $h_m$ , the non-dimensional mountain height is 4.9, well into the flow-around regime according to previous studies (e.g. Smith 1989). Therefore, severe blocking and wind turning should be expected to the north-west of the Alps. However, it should be pointed out that the Payerne sounding is launched only about 50 km upstream of the Alpine massif, and is probably influenced by upstream perturbations, in which case the non-dimensional mountain height may be overestimated. Above the stable layer, the wind direction is northerly and wind speed is much stronger ( $>20 \text{ m s}^{-1}$ ). Corresponding to this increase of wind speed and decrease of stability above the stable layer, the Scorer parameter decreases with increasing altitude between 2 and 4 km. The 0600 and 1800 UTC soundings from Payerne (not shown) indicate that the large-scale flow is fairly steady during the 12-hour period. Both the wind speed and potential temperature profiles show little change from 0600 to 1800 UTC.

The Buchs-Grab 1200 UTC sounding indicates that a stable layer is located between 3 and 5 km, which is much higher than observed at Payerne. Below the stable layer, the northerly wind component is small ( $<5 \text{ m s}^{-1}$ ). The wind direction is north-westerly, suggestive of flow splitting due to blocking. Above the stable layer, wind speed at Buchs-Grab is about 30% stronger than measured at Payerne and the wind direction (not shown) is northerly as well. Accordingly, a sharp decrease of Scorer parameter with increasing altitude around 3 km is evident. The strong variation of wind speed along the Alpine crest is consistent with the rapid-scan analysis. Similarly, the 0600 and

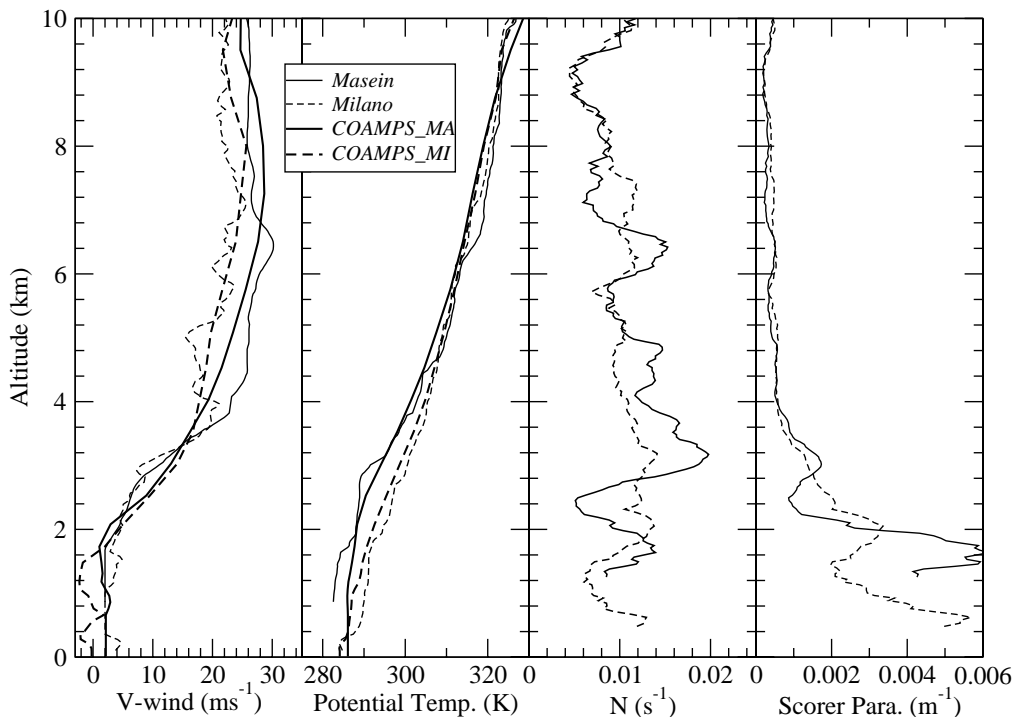


Figure 6. As Fig. 5, but for Masein and Milano.

1800 UTC Buchs-Grab soundings (not shown) indicate that the large-scale flow is fairly steady.

Profiles of  $v$  wind component, potential temperature, buoyancy frequency, and Scorer parameter derived from soundings launched from Masein ( $46.71^{\circ}\text{N}$ ,  $9.43^{\circ}\text{E}$ , 865 m) and Milano ( $45.43^{\circ}\text{N}$ ,  $9.27^{\circ}\text{E}$ , 107 m) at 1200 UTC on 8 November 1999 are shown in Fig. 6. In general, the  $v$  wind and potential temperature profiles derived from the Masein and Milano soundings are similar to those derived from the Buchs-Grab sounding. For all three soundings, there is a stable layer located in the middle troposphere, which separates a less stable and nearly stagnant layer below and the upper troposphere with strong wind speed. In fact, the three radiosonde stations, Buchs-Grab, Masein, and Milano, are located to the north, in the middle, and to the south of the Alps, respectively (see Fig. 2 for locations), approximately aligned with the large-scale wind direction (i.e. northerly). Considering that the large-scale flow was fairly steady during the observational period, comparisons among soundings from the three stations to some degree illustrate the modification of synoptic flow by the complex Alpine massif. The 1200 UTC Buchs sounding reveals a stable layer located between approximately 3.3 and 5 km. The Masein sounding shows a stable layer based at 3 km, which is lower and more stable than observed at Buchs-Grab. The 3–5 km layer at Masein is warmer than observed at Buchs. For example, at Masein, the altitude of  $\theta = 295$  K is about 700 m lower than observed at Buchs, indicating a significant descent over a distance of approximately 150 km. Correspondingly, the wind speed at Masein is stronger between 2 and 5 km as well. It is interesting that the two potential temperature profiles (i.e. Buchs and Masein) are almost identical below 3 km, implying weak vertical motion in

the lowest 3 km. The base of the stable layer descends to 1.8 km at Milano, which is 1.5 km lower than observed at Buchs-Grab. Below the stable layer, the Milano sounding shows the presence of a near-neutral layer, possibly an indication of a different mass source. The air in the neutral layer is approximately 8 K warmer than the air at Buchs-Grab and Masein at corresponding altitudes. The stagnation layer (defined by the wind speed less than  $5 \text{ m s}^{-1}$ ) is still present.

In summary, soundings in the Alpine area indicate that the large-scale flow was fairly steady between 0600 and 1800 UTC on 8 November 1999. The stratification and wind speed show strong variations along the Alpine ridge. A deep stagnant layer is located in the central Alps underneath a stable layer. The non-dimensional mountain heights derived from soundings to the north of the Alps are fairly large, indicative of strong blocking upstream of the Alps. Comparison of three soundings aligned approximately along the wind direction indicates cross-mountain air descent and warming aloft. The Milano sounding reveals very weak flow below 2 km, which implies the presence of mountain wakes in the Po valley. Corresponding to the strong wind speed in the less stable upper troposphere, all four soundings reveal a sharp decrease of Scorer parameter above the stable layer, which is necessary for the existence of trapped waves.

(c) *Parcel displacement and SABL backscatter*

With linear and steady-state assumptions, the vertical displacement of air parcels at a flight level can be derived from aircraft data using

$$\eta(x) = \int_0^x (w'/U) dx \quad (2)$$

where  $w'(x) = w(x) - \bar{w}$  and  $U$  is the horizontal velocity averaged over three points. The reference points ( $x = 0$ ) are the starting points of each leg. The mean vertical motion has been removed to force the vertical displacement approximately back to zero at the end point. A Lanczos filter (Duchon 1979) is applied to filter out scales less than 2 km and larger than 200 km.

The returns of the Electra lidar (SABL) along two legs (2 and 4) are plotted on Fig. 7, along with vertical displacement  $\eta(x)$  derived from aircraft data, and the terrain beneath interpolated from a 100 m resolution dataset. Figure 7(a) shows the SABL backscatter from the Electra leg 2, terrain along the flight leg, and parcel vertical displacement derived from two Electra legs, ten UK C-130 legs, and six DLR Falcon legs. The actual flight transverses may have deviated slightly from the planned primary track shown in Fig 2. The vertical displacement data indicate a remarkable repetition among different legs, which suggests that waves were quite steady during the observational period. The displacement field also shows strong vertical coherence. Several plausible phase lines are drawn through wave troughs assuming that the waves are stationary and excited by the irregular terrain below.

Two distinctive wave modes are evident with horizontal characteristic lengths of 13 km (indicated by dashed phase lines) and 8 km (indicated by dotted phase lines). The shorter waves decay with altitude and the amplitude of the longer waves show little change from the 5.5 km level to the 8.2 km level.

In unshered flow with a constant buoyancy frequency  $N$ , the displacement due to a stationary wave in an  $x$ - $z$  plane can be written as

$$\eta(x, z) = \eta_0 \exp\left(\frac{z}{2H_s} + ikx + imz\right), \quad (3)$$

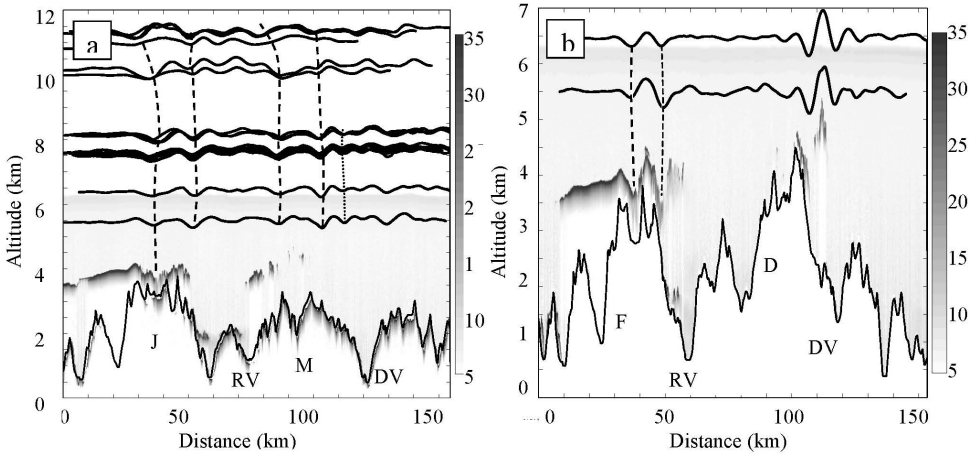


Figure 7. SABL backscatter coefficient (grey scale) along two Electra transverse: (a) leg 2 and (b) leg 4. Vertical displacements computed from the flight-level data using Eq. (2) are shown as solid lines. Some plausible phase lines are indicated by dashed or dotted lines. The terrain is plotted below, with peaks and valleys of interest labelled: Jungfrau (J), Rhone valley (RV), Matterhorn (M), Aosta valley (DV), Finsteraarhorn (F) and Dufourspitz (D).

where  $k$  is the horizontal wave number and the vertical wave number  $m = \sqrt{l^2 - k^2}$ . The other symbols are the density scale height,  $H_s$ , and the displacement at a reference point,  $\eta_0$ . If  $l > k$ ,  $m$  is real, and Eq. (3) represents a propagating wave with a phase line tilting at an angle of  $\tan^{-1}(k/m)$ . If  $l < k$ ,  $m$  is imaginary, and Eq. (3) represents an evanescent wave whose phase line should be vertically oriented and amplitude varies with altitude as

$$\exp\left(\frac{z}{2H_s}\right) \cdot \exp(-mz).$$

The nearly vertical phase line and the slow variation of wave amplitude with altitude suggested  $k \simeq l$  for the longer waves. The Payerne 1200 UTC sounding shows that the Scorer parameter  $l \simeq 0.00042 \text{ s}^{-1}$  between 6 and 10 km. Correspondingly, waves with wavelengths shorter than approximately 15 km are probably evanescent. According to the linear wave theory, for 2D evanescent waves, the two velocity perturbations should be in quadrature. Further analysis of the Electra and C-130 data indicates that  $v$  and  $w$  are approximately in quadrature for the longer waves. Therefore, the longer waves are probably evanescent waves.

Despite the strong northerly flow over the Alpine high terrain, the measured wave amplitudes are fairly small. The maximum peak-to-trough amplitude (PTA) of the displacement is less than 0.5 km. According to both radiosonde and Falcon *in situ* measurements, the tropopause is located approximately at 10.5 km. The lowest Falcon flight level is within the troposphere and the upper level is in the stratosphere, as indicated by a sharp increase of stratification and decrease of water vapour between the two levels. The phase lines tilt rapidly backwards near 11 km, associated with the sudden increase of static stability across the tropopause.

The most intense SABL backscatter should be associated with cloud water. Despite significant relief underneath, the cloud top upstream of Jungfrau is fairly flat, a likely indication of flow blocking. A cloud trough is located over Jungfrau, which is in phase with the wave above. The descent associated with wave troughs appears too weak to dissipate clouds completely. A 25 km wide clear zone is located over the Rhône valley,

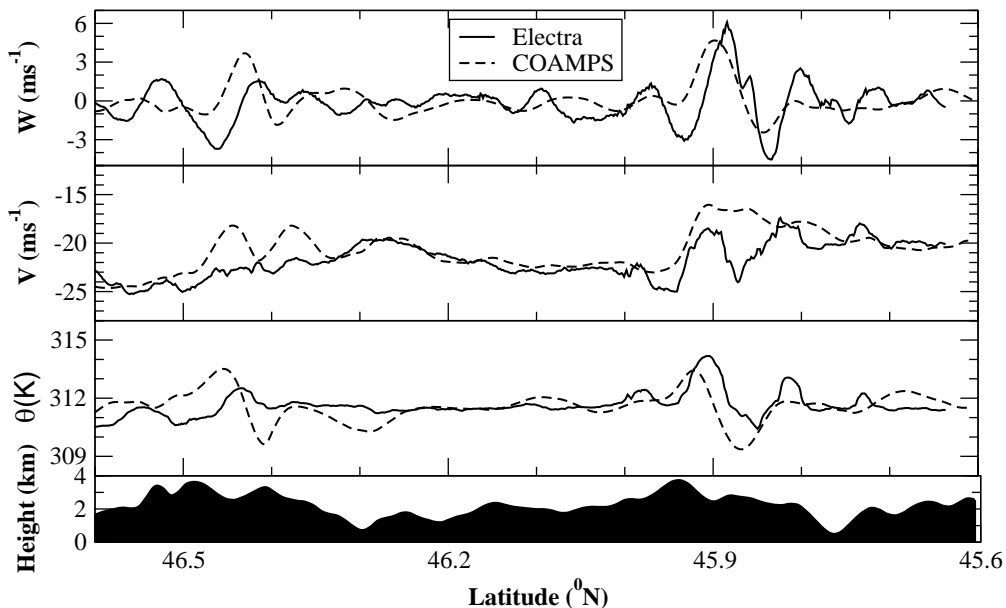


Figure 8. The vertical motion  $w$ , meridional wind component  $v$ , and potential temperature  $\theta$ , measured by the NCAR Electra along its third transverse. The corresponding curves derived from the COAMPS grid 4 mesh are plotted for comparison. The model terrain is shown below.

probably associated with lee-side descent which is consistent with GPS dropsonde data. GPS dropsondes from both the Electra and C-130 indicate the presence of a strong jet and relatively warm air over the lee slope of Jungfrau. A strong SABL return is detected at approximately 1.8 km in the valley, which is likely to be associated with high aerosol concentration in the stagnant air trapped in the lower valley. Figure 7(b) shows the SABL return from the fourth Electra leg and vertical displacement derived from Electra transverses 3 and 4, which pass the peaks of Finsteraarhorn and Dufourspitze. Two distinctive wave trains are evident, one over Finsteraarhorn with one crest and two troughs and a maximum PTA of 0.6 km, and a second one over Monte Rosa with three troughs and a maximum PTA of 0.9 km. The respective wavelengths are 13 km and 11 km. The two primary wave crests and the secondary wave in the lee of Monte Rosa are also evident in the rapid-scan Hovmüller diagram (Fig. 4(a)).

The SABL backscatter indicates a possible signature of blocking upstream of Finsteraarhorn, the presence of aerosol-rich air in the lower part of the Rhône valley, and relatively large-amplitude waves over the two peaks. The displacement maximum in the lee of Monte Rose is in phase with a lenticular cloud below. This cloud was clearly seen also on the AVHRR image (Fig. 3(b)). A photograph of this lenticular cloud (not shown), taken from the south of Monte Rosa, indicates that this dish-like lenticular cloud is highly three-dimensional. The 3D character of the lenticular cloud is consistent with the Electra observations; waves sampled along track WT2 are significantly stronger than those sampled along tracks WT1 and WT3, located only several kilometres away.

The vertical motion,  $v$  wind component, and potential temperature sampled by the Electra along its third leg are plotted in Fig. 8. For the large-amplitude wave over the lee of Monte Rosa, the perturbations of  $v$  and  $w$  are approximately in quadrature (i.e. no momentum flux), and the perturbations of  $v$  and  $\theta$  are approximately in phase, indicating that this wave is probably evanescent and decreasing aloft.

(d) *Constant-volume balloons*

On 8 November 1999, four constant-volume balloons (CVBs) were released from Diepolsau, Switzerland (47.37°N, 9.66°E, 411 m) to measure gravity waves between the 3 and 5 km levels (Bougault *et al.* 2001). The wind and potential temperature measured by a CVB launched at 1107 UTC are plotted in Fig. 9. The flight altitude is approximately 3400 m and the trajectory orientation is approximately north–south. The mean quantities have been removed from measured potential temperature and velocity components. Then the perturbations are separated into fast perturbations (scales less than 20 km) and slow perturbations (scales larger than 20 km) using Discrete Fourier Transform. It should be noted that there were some instrumental problems between 46° and 46.4°N.

From the slow potential perturbation curve, the cross-Alpine warming is evident. Between 47.2° and 45.8°N, while the balloon altitude is almost constant (~150 m descent), the potential temperature increases by 6 K, indicative of strong flow descent over the lee slope of the main Alpine massif. Rapid variation of potential temperature occurs between 46.5° and 45.9°N over the lee slope of the main Alpine ridge, probably associated with the development of a downslope wind storm. From 45.8° to 45.2°N, the potential temperature decreases slightly (~1 K), the westerly component of the wind increases by 4 m s<sup>-1</sup>, the northerly component decreases by 6 m s<sup>-1</sup>, and the relative humidity (not shown) decreases accordingly.

Between 47.2° and 46.4°N, there is a well-defined wave train with a dominant wavelength of 5.8 km according to spectrum analysis. The maximum PTAs of potential temperature and vertical motion are 5 K and 4 m s<sup>-1</sup>, respectively. Further downstream, there are some weaker waves with a longer horizontal scale (10 ~ 14 km). Due to time lags in the balloon response, we have not analyzed the phase relations between different balloon-derived variables.

#### 4. COAMPS REAL-DATA SIMULATIONS

The atmospheric component of the NRL's COAMPS (Hodur 1997) was used to simulate this northerly föhn event. COAMPS is a fully compressible, non-hydrostatic model with a suite of physical parametrizations such as cloud microphysics, cumulus, and radiation. The prognostic equation for turbulent kinetic energy (TKE) is based on the level 2.5 formulation of Mellor and Yamada (1974).

The computational domain for the present study was configured with four horizontally nested grids of 87 × 87, 121 × 121, 151 × 151 and 211 × 211 points. The corresponding horizontal spatial resolutions ( $\Delta x$ ) are 27, 9, 3, and 1 km, respectively. The topographic data was taken from a 1 km resolution global dataset. The fourth mesh is large enough to include all the flight tracks. High spatial resolution is used to resolve small-scale features such as evanescent waves. There are 55 vertical levels and the terrain-following coordinate is stretched with  $\delta Z_{\min} = 20$  m near the surface. The model top is at 31 km with Rayleigh damping applied to the upper 11 km. The initial and boundary conditions are specified using the Naval Operational Global Atmospheric Prediction System (NOGAPS) analysis. An increment update data assimilation procedure that enables mesoscale phenomena to be retained in the analysis increment fields is used for model initialization. For the purpose of model validation, the real-time simulation is compared with radiosonde data, *in situ* measurements, and SABL backscatter in this section.

The profiles of the meridional wind speed and potential temperature extracted from the COAMPS 1 km grid are included in Figs. 5 and 6 to compare with the 1200 UTC

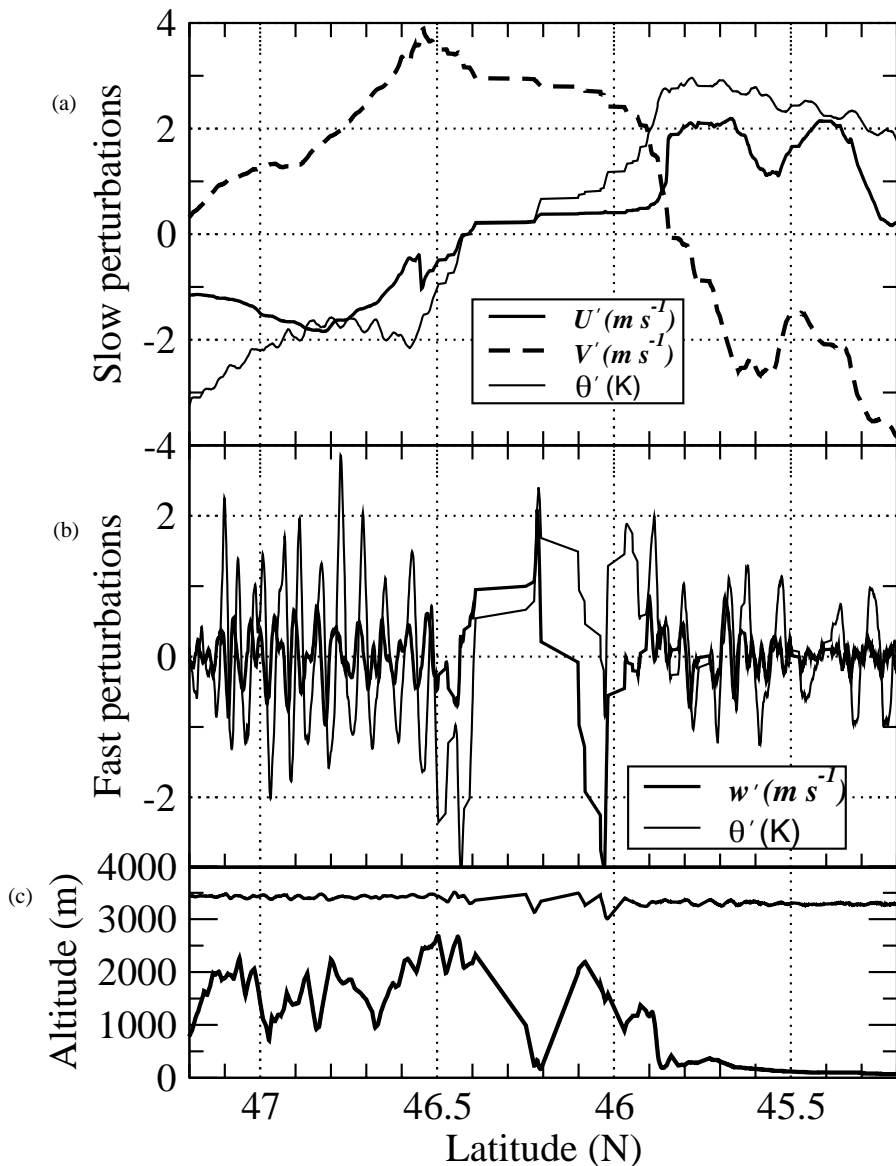


Figure 9. Plots of (a) slow perturbations of two horizontal wind components and potential temperature and (b) fast perturbations of vertical motion and potential temperature, derived from measurements by a constant-volume balloon launched at 1107 UTC on 8 November 1999, and (c) shows the balloon and terrain heights.

Payerne, Buchs-Grab, Masein and Milano soundings. The profiles are derived from the model points that are closest to the sounding station locations. The advection of sondes is ignored. For all four soundings, the model potential temperature profiles agree very well with observations. The model realistically reproduces the three-layer structure of the troposphere, namely, a less stable layer below, a stable layer located in the middle troposphere, and a less stable layer in the upper troposphere. In general, the model profiles are smoother due to the lower vertical resolution relative to soundings. At Payerne, Masein, and Milano, the agreement between the model wind profiles and

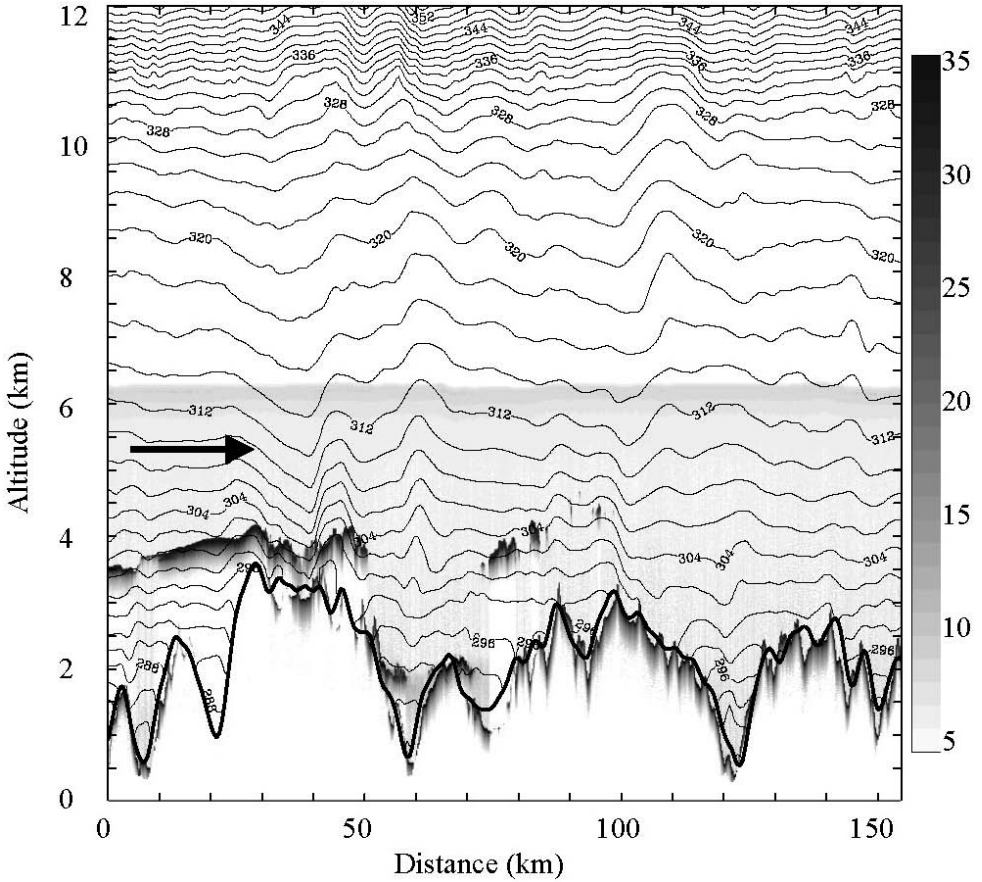


Figure 10. Isentropes from the COAMPS fourth grid mesh ( $\Delta x = 1$  km) at 1200 UTC on 8 November 1999, interpolated onto a vertical cross-section approximately along the second Electra transverse. Wind is from left to right. The corresponding SABL backscatter is shown as grey shading.

observations is quite good. Again, the soundings show more details due to their higher vertical resolution. At Buchs-Grab, above 3 km amsl, the model meridional wind agrees well with observations. However, the model meridional wind speed is stronger than observed in the lowest 3 km.

The vertical motion,  $v$  wind component, and potential temperature from the third Electra flight leg are compared with model data (Fig. 8). The 1 km model data are interpolated to the corresponding flight altitudes, latitudes and longitudes. The vertical motion curves indicate that COAMPS captures the relatively large-amplitude wave over the lee of Monte Rosa with a correct wavelength, although the model wave amplitude is smaller and the model wave crest is located a little more upstream. The model indicates that the  $v$  wind component weakens over the lee of Monte Rosa by  $6\text{--}7\text{ m s}^{-1}$ , which is in agreement with observation.

The potential temperature and terrain from the COAMPS fourth grid mesh ( $\Delta x = 1$  km) at the time approximately corresponding to each Electra flight transverse are interpolated to the SABL cross-sections. Figure 10 shows the SABL backscatter along the second Electra transverse with the interpolated COAMPS potential temperature contours and model terrain superposed. The COAMPS simulation indicates a stable

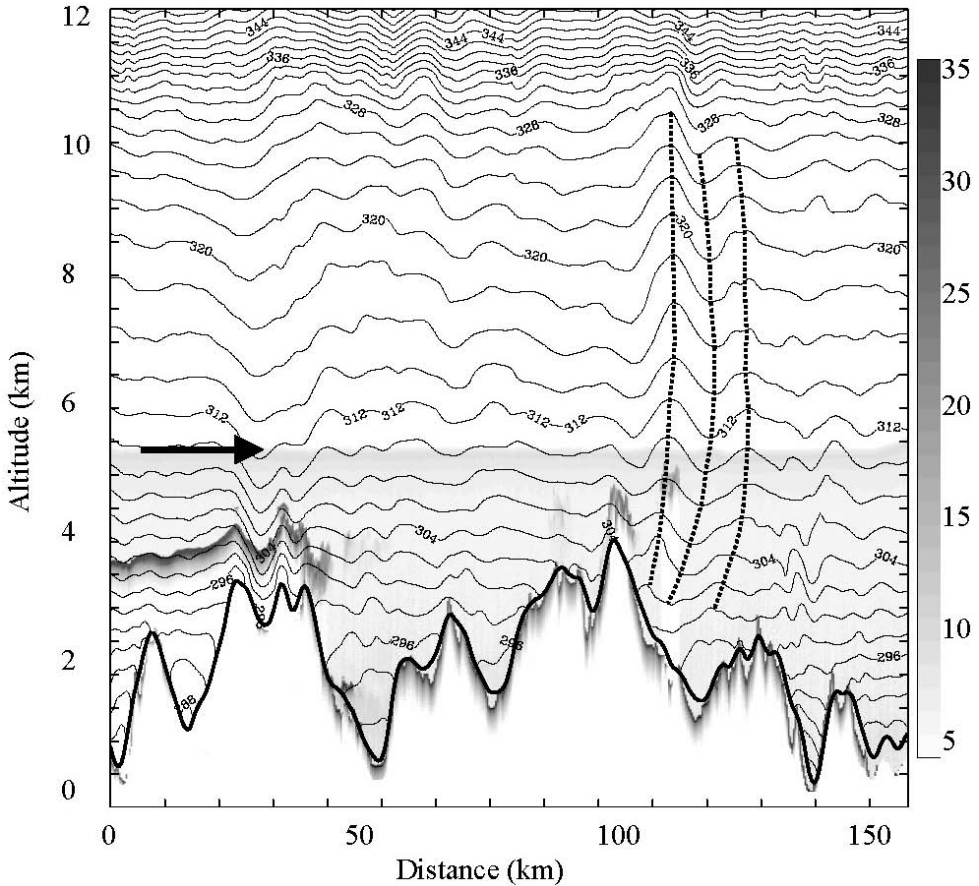


Figure 11. As Fig. 10, but for the fourth Electra transverse. The three dotted lines are plausible phase lines of two waves located downstream of Monte Rosa.

layer located approximately below 5 km with a less stable layer above it. The model terrain (bold line) matches the SABL backscatter patterns from the surface reasonably well. Upstream of the first high peak, the isentropes are rather flat. The 300 K and 302 K contour lines also follow the cloud top (indicated by SABL backscatter). The intercept of the isentropes ( $\theta < 296$  K and  $z < 3$  km) with Jungfrau suggests flow blocking to the north of the Alps. Isentropes in the Rhone valley are fairly flat and follow the boundary-layer top (indicated by SABL backscatter) closely. COAMPS captures the two primary wave troughs downstream of Jungfrau with a slightly longer wavelength ( $\sim 14$  km) and larger amplitude (PTA  $\sim 0.7$  km) than observed.

The vertical section along the third Electra transverse is shown in Fig. 11. Over Jungfrau, the COAMPS potential temperature field shows two wave troughs with horizontal scales of 5 and 10 km at the 4 km level, which are likely to be a response to the fine-scale terrain features. The model-simulated isentropes match the cloud troughs indicated by the SABL backscatter fairly well. The two waves merge into one wave aloft, probably due to dispersion. Over the lee of Monte Rosa, the two isolated lenticular clouds coincide with two wave crests in the isentropes. The wavelength is approximately 11 km at 6 km height, which agrees with Electra observations. However, the PTA at 6 km is about 0.7 km which is slightly smaller than the observed wave amplitude (i.e. 0.9 km).

The corresponding wave number is larger than the Scorer parameter at the 6 km level in the vicinity of Payerne computed from COAMPS fourth grid data, which implies that the model-simulated waves should be evanescent as well. Downstream from both Jungfrau and Monte Rosa there are some shorter evanescent waves, which decay rapidly with increasing altitude.

The dotted lines in Fig. 11 indicate plausible phase lines for waves in the lee of Monte Rosa. Between 5.5 and 8.5 km, these phase lines show little tilting as observed by the aircraft, which suggests that  $|m| \sim 0$ . Downstream of Monte Rosa, the three phase lines clearly show forward tilting below 5.5 km and backward tilting above 8.5 km. According to mountain-wave theory, the wave group velocity is related to the phase line tilt. The forward tilting of the phase line indicates a downward propagation of wave energy (along the group velocity direction) and the backward tilting indicates upward propagation of wave energy (e.g. Smith 1979). The downward wave energy propagation is likely caused by wave reflection aloft associated with a sharp decrease of Scorer parameter and wave absorption at the bottom associated with the stagnant layer as suggested by Smith *et al.* (2002). Wave energy leaks aloft as indicated by the backward tilting of phase lines.

In general, the agreement between observations and the COAMPS simulation is reasonable. COAMPS also indicates flow descent across the Alps in the lower troposphere, which is in qualitative agreement with CVB measurements. For example, the 304 K isentrope starts approximately at 4.5 km and descends to 3.6 km, a descent of 0.9 km over a horizontal distance of about 150 km.

## 5. DISCUSSION

Observational analysis indicates the presence of several dynamical processes during this northerly föhn event, namely, windward blocking, gravity waves, cross-Alps flow descent, and lee-side wake formation. Some aspects of the relevant dynamical processes and interactions among them will be further discussed in this section based on the diagnosis of the COAMPS real-data simulation and two sensitivity tests with terrain heights of one half and one quarter of the control run (hereafter referred to as half-terrain and quarter-terrain runs, respectively).

### (a) Windward blocking

The blocking of low-level cold air is known as one of the mechanisms for föhn formation. According to radiosonde analysis, the non-dimensional mountain height is well above unity during the observational period, indicative of severe blocking. A nearly stagnant layer up to 3 km in the central Alps is identified through the analysis of radiosondes and rapid-scan images. To isolate the effect of the Alpine ridge in stagnant-layer formation, in addition to the real-data simulation half-terrain and quarter-terrain runs have also been conducted. As an example, the isentropes,  $v$  wind component and water vapour mixing ratio in the cross-section through 9.5°E are shown in Fig. 12 for the three simulations. Low-level blocking is evident in the full-terrain simulation, as indicated by the interception of the isentropes by the terrain. The top of the blocked layer (i.e.  $\theta = 296$  K) is at  $\sim 3$  km, below which the northerly component of the wind is less than  $8 \text{ m s}^{-1}$ . Below 1.5 km, a near-stagnant layer is located upstream of the main massif, with speed less than  $4 \text{ m s}^{-1}$ . Figure 12(b) indicates that the air below 3 km is more moist to the north of the Alps, and clearly blocked by the main Alpine crests. To the south, the air below 3 km is much drier in terms of both mixing ratio and relative humidity, and is probably from a different air mass. For the half-terrain simulation, the

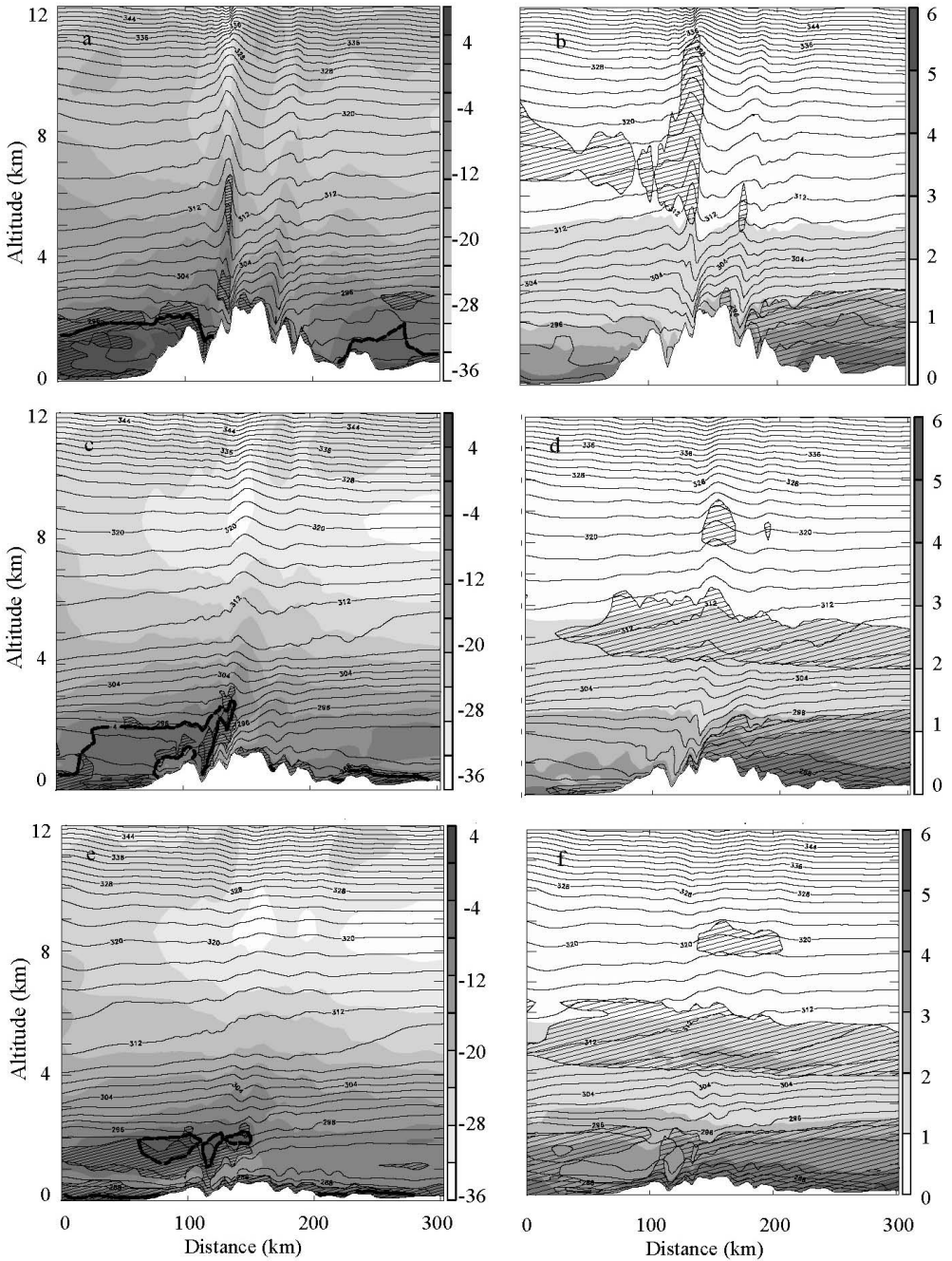


Figure 12. Cross-section through  $9.5^{\circ}\text{E}$  derived from COAMPS third grid mesh for (a)  $v$  component of the wind (grey scale,  $\text{m s}^{-1}$ ) and (b) water vapour mixing ratio (grey scale,  $\text{g kg}^{-1}$ ). Both also show equivalent potential temperature (contours, K). Note that here the wind is from the right. In (a), regions with Richardson number less than 2 are hatched and regions with  $v$  greater than  $-4 \text{ m s}^{-1}$  are indicated by heavy contours. In (b), regions with relative humidity greater than 65% are hatched. Results from the half-terrain simulation are shown in (c) and (d), and the quarter-terrain simulation in (e) and (f), following the conventions in (a) and (b).

top of the blocked layer is at  $\sim 1$  km. Although some moist air is advected to the lee side, the low-level clouds are clearly confined to the windward side. For the quarter-terrain simulation, while the flow below the stable layer is still relatively slow ( $\sim 12$  m s $^{-1}$ ), there is no clear indication of terrain-related blocking. Accordingly, clouds appear in the lee of the Alps associated with moisture advection and less descent over the lee slope.

To estimate the role of the stable layer in windward blocking, we use the shallow-water flow approximation. For a single-layer flow with depth  $D$ , the blocking condition is given by  $h_c/D = 1 + 0.5Fr^2$  (Schär and Smith 1993), where  $h_c$  is the critical mountain height to have stagnation, and  $Fr = U/\sqrt{g'D}$  is the Froude number. The Froude number can be estimated from the upstream soundings. If we use  $D = 3000$  m, the reduced gravity  $g' = \theta'g/\theta = 10 \times 9.8/300 = 0.33$  m s $^{-2}$ , and  $U = 5$  m s $^{-1}$ , we have  $Fr = 0.16$  and  $0.5Fr^2 \ll 1$ . The averaged height of the main Alpine ridge is about 3 km, which is enough to block the moist layer below the inversion. According to Pierrehumbert and Wyman (1985), in the 2D limit, the horizontal dimension of the blocked zone is given by  $d = Nh_m/f \simeq 0.012$  s $^{-1} \times 3000$  m/ $10^{-4}$  s $^{-1} = 360$  km. According to shallow-water theory, the Rossby deformation radius is given by  $R = C/f \simeq 32$  m s $^{-1}/10^{-4}$  s $^{-1} = 320$  km, where  $C$  is the shallow-water wave speed as estimated above. The estimated deceleration zone from the COAMPS outer-grid mesh ( $\Delta x = 27$  km) is of the order of 250 km, which is consistent with shallow-water theory and linear theory by Pierrehumbert and Wyman (1985).

### (b) Flow descent and föhn window

Analysis of the CVB data and radiosondes indicates cross-Alp flow descent, which is consistent with the presence of the föhn window in the lee of the Alps. The cross-sections from the COAMPS simulations indicate strong baroclinicity; the air is warmer to the south of the Alps in the lower troposphere as indicated by the tilting of isentropes (Fig. 12(a)). If we assume that the flow is steady and the wind direction is northerly, the isentropes indicate a gentle large-scale flow descent in the lower troposphere and a sharper descent over the lee slope. The large-scale descent shows moderate sensitivity to the mountain height. The sharp descent over the lee slope associated with the development of the wind storm is significantly weaker for lower terrain, apparently controlled by the terrain slope underneath.

The trajectories of several parcels launched from (48°N, 9.5°E) at 0700 UTC are computed using the 3D wind field derived from the control simulation. Trajectories terminate when they hit terrain or when the time reaches 1200 UTC. Figure 13 shows the altitudes of the parcels as a function of distance from the starting point. Parcels released below 3 km are blocked to the north of the Alps. Parcels released from between approximately 3 and 6 km tend to descend at two distinctive scales: slow descent over a horizontal scale of 300–400 km and sharp descent over the lee of major crests over a horizontal scale of around 10 km. Relative to the parcel released from the 4 km level, the parcel released from the 5.5 km level experiences stronger descent, which probably accounts for the thinner and more intense stable layer to the south of the Alps observed by radiosondes. The sharp descent occurs over the lee of high peaks associated with a sudden increase of the wind speed. Further downstream, parcels recover their altitudes through a hydraulic jump, a zone characterized by sharp ascent of parcels and TKE generation.

The parcels released from the 6.5 and 7.5 km levels experience a sudden ascent over the crest and a slow descent in the lee, which resembles the inertia–gravity

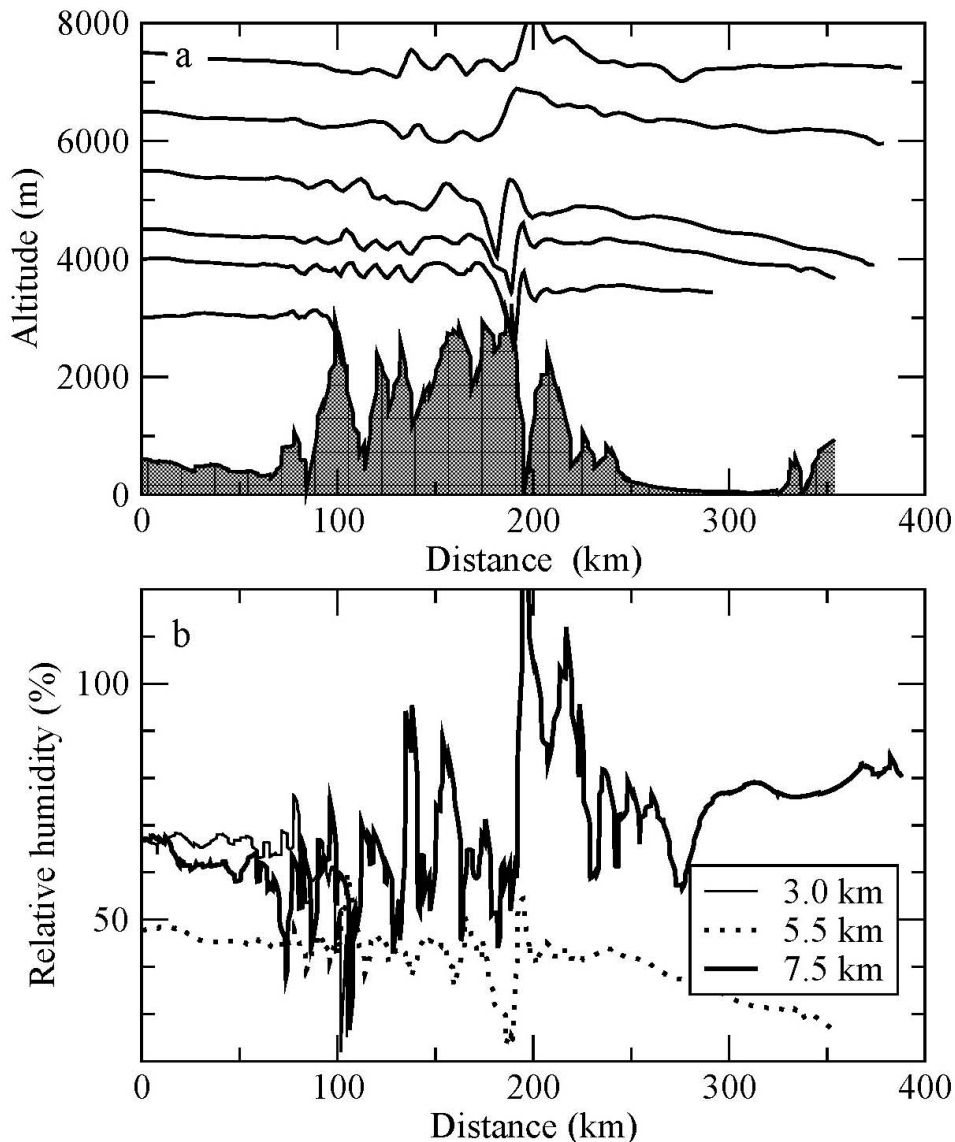


Figure 13. (a) Plot of altitude versus horizontal distance for parcels released from (48°N, 9.5°E) at 0700 UTC on 8 November 1999. The terrain underneath the parcel released at 4.5 km is shown below. (b) Plot of relative humidity versus horizontal distance for three parcels released from the same point at three altitudes (3, 5.5 and 7.5 km).

wave solutions described by Queney (1948). The relative humidity around 7 km is significantly increased in the lee associated with the sudden ascent and slow descent pattern, which is consistent with the AVHRR image (Fig. 3(a)). The increase of relative humidity in the lee of the Alps around the 7 km level is also evident in Fig. 12(b), and absent from the half- and quarter-terrain runs, indicating that this phenomenon is controlled by the high Alpine ridge. Parcels released at a later time indicate an increase of moisture at low level below the inversion and decrease of moisture aloft near the 7 km

level with time, which is consistent with the widening of the föhn window observed by satellites. Parcels released from the Po valley below 2 km indicate that the low-level warm air in the Po valley has an origin from the south-east, probably under the influence of the mid-tropospheric cyclone located over Sicily.

(c) *Waves and wave breaking*

Both observations and modelling indicate the presence of trapped waves with wavelength ranging from 5.8 to 13 km associated with a sharp decrease of Scorer parameter above the stable layer. These waves are steady and persistent. The fast decay of trapped waves with downstream distance in the lee of the Alpine ridge is probably associated with wave absorption by the stagnant flow underneath, as suggested by Smith *et al.* (2002).

For all three simulations, the isentropes ascend sharply immediately downstream of the lee-side descent. Associated with the isentropic ascent, a zone with small Richardson number is present, which separates strong downslope flow from weak wake flow, indicative of low-level wave breaking or a hydraulic jump. This observation is consistent with Flamant *et al.* (2004). They concluded that the secondary PV banners observed in the Po valley in the afternoon of 8 November were associated with low-level wave breaking over the Alps.

The occurrence of hydraulic jumps is associated with the presence of a stable layer between 3 and 5 km, which acts to decouple the low-level flow from the air above (Schär and Smith 1993). An estimation based on the COAMPS vertical cross-sections indicates that flow over the lee slope is supercritical until a jump occurs. For example, from Fig. 12(a), the layer between 296 K and 302 K descends over the lee slope of the Berner Alpen and ascends sharply afterwards. Over the lee slope, the stable-layer depth is approximately  $H = 800$  m, the reduced gravity  $g' = \theta'g/\theta_0 = 6 \text{ K} \times 9.8 \text{ m s}^{-2}/300 \text{ K} \simeq 0.2 \text{ m s}^{-2}$  and the corresponding shallow-water wave speed is  $\sqrt{g'H} = 12.6 \text{ m s}^{-1}$ . The wind speed is approximately  $16 \text{ m s}^{-1}$ , which yields a Froude number of  $\sim 1.3$ .

The vertical profile of the domain-averaged TKE provides further evidence for possible low-level wave breaking (Fig. 14). Three distinctive maxima are evident. The lowest maximum is clearly associated with the turbulent boundary layer. Further analysis indicates that the second maximum approximately located between 1 and 3 km is associated with low-level wave breaking or hydraulic jumps over the lee slope of the Alpine ridge and the third maximum located in the lower stratosphere is associated with mountain-wave breaking aloft.

(d) *Effective mountain height and mountain drag*

One interesting question concerns the impact of low-level flow blocking and wave breaking on mountain waves and drag. To address this issue, the profiles of the domain-integrated meridional component of the horizontal momentum fluxes are shown in Fig. 15. The momentum flux,  $MF$ , is computed using

$$MF(z) = \overline{\rho(z)} \iint v'w' \, dx \, dy, \quad (4)$$

where  $\overline{\rho(z)}$  is air density and  $v'$  and  $w'$  are velocity perturbations. According to linear theory, mountain drag is proportional to the square of the mountain height. For the purpose of comparison, the momentum fluxes derived from the half-terrain and quarter-terrain simulations are multiplied by factors of 4 and 16, respectively. For all three

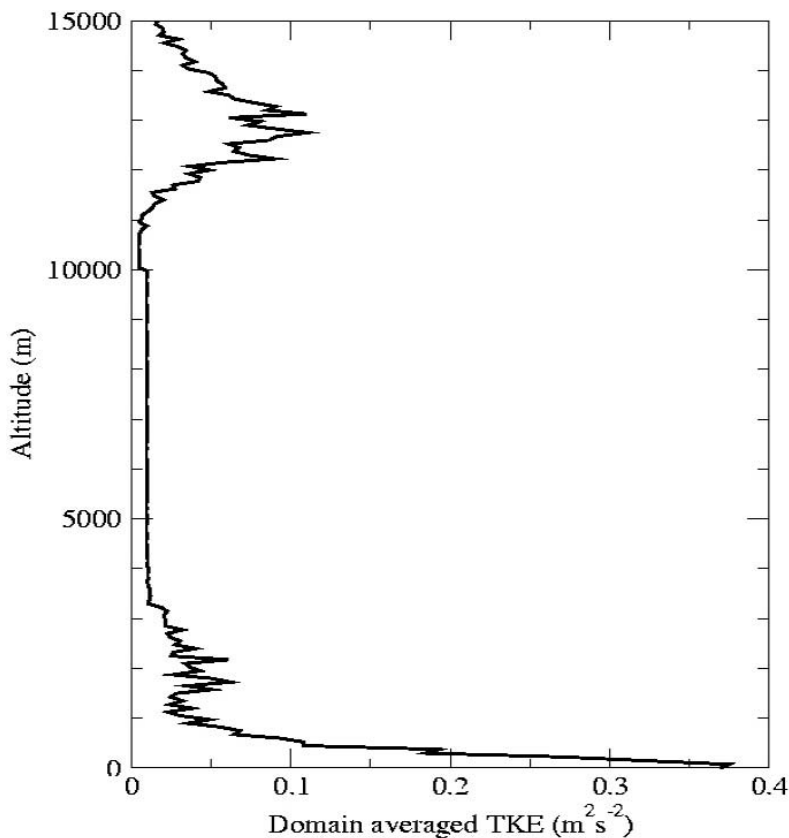


Figure 14. Profile of turbulent kinetic energy averaged over the COAMPS third grid mesh. The vertical coordinate here is the altitude above ground.

simulations, the momentum flux increases with altitude until a maximum is reached at approximately the corresponding mountain peak level. Further aloft, a sharp decrease occurs, probably associated with low-level wave breaking or hydraulic jumps. The dissipative nature of hydraulic jumps tends to reduce upward transport of wave energy and therefore reduces the wave amplitude aloft. For both the half-terrain and quarter-terrain simulations, the momentum flux is fairly constant with altitude, as expected in the absence of wave breaking. For the full-terrain simulation, there is a second sharp decrease of momentum flux at about 12–15 km, probably associated with wave breaking in the lower stratosphere, which is consistent with the TKE profile (Fig. 14). Apparently, the momentum flux maxima are not proportional to the square of mountain height as suggested by linear theory; instead, they are approximately proportional to  $h^{3/2}$ , i.e. drag  $D = Ah^{3/2}$ . The slower increase of the momentum flux with mountain height is probably due to mountain blocking effects. The dependence of momentum flux on mountain height and blocking level has been demonstrated in Smith *et al.* (2002) using a linear model. It was shown that the momentum flux is very sensitive to the depth of the blocked layer, or cut-off height.

The importance of proper representation of mountain drag in global circulation models has been well recognized (Lindzen 1981; Kim *et al.* 2003, among many others).

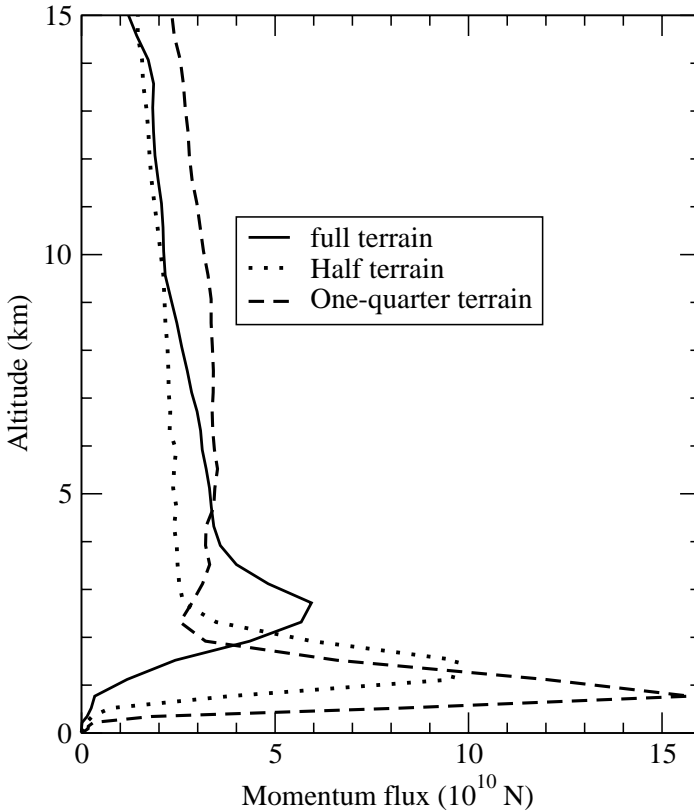


Figure 15. Profiles of momentum flux integrated over the COAMPS third grid mesh for the full terrain, half-terrain and quarter-terrain runs (see text for details). The flux is multiplied by 4 for the half-terrain run and by 16 for the quarter-terrain run.

Both this study and Smith *et al.* (2002) imply that the presence of flow blocking and a stagnant layer may significantly decrease mountain-induced momentum flux or drag. It is critical to determine the effective mountain height in order to properly parametrize mountain drag, especially the drag associated with major mountain barriers. Here we derive an empirical formula to estimate the effective mountain height based on the three simulations.

According to linear theory, the vertical momentum flux or drag  $D \propto ah^2$  (Smith 1979), where  $h$  is terrain height and  $a$  is a terrain horizontal dimension. For a simple 3D cone, we have  $D \propto h^3$ . Therefore, for cone-shaped terrain with a height  $h$ , and a blocked layer of depth  $h_b$ , the drag can be written as  $D = Bh_e^3$ , where the effective mountain height  $h_e = h - h_b$ . If we define  $h_c = A^2/B^2$ , and combine the two drag formulae, we obtain  $h_b = h(1 - \sqrt{h_c/h})$ . In non-dimensional form, the effective mountain height for high terrain (i.e.  $\hat{h} > 1$ ) is

$$\hat{h}_e = \sqrt{\hat{h}}, \quad (5)$$

where  $\hat{h}_e = h_e/h_c$  and  $\hat{h} = h/h_c$ . Equation (5) provides a convenient way to estimate the blocking effect in mountain-drag reduction.

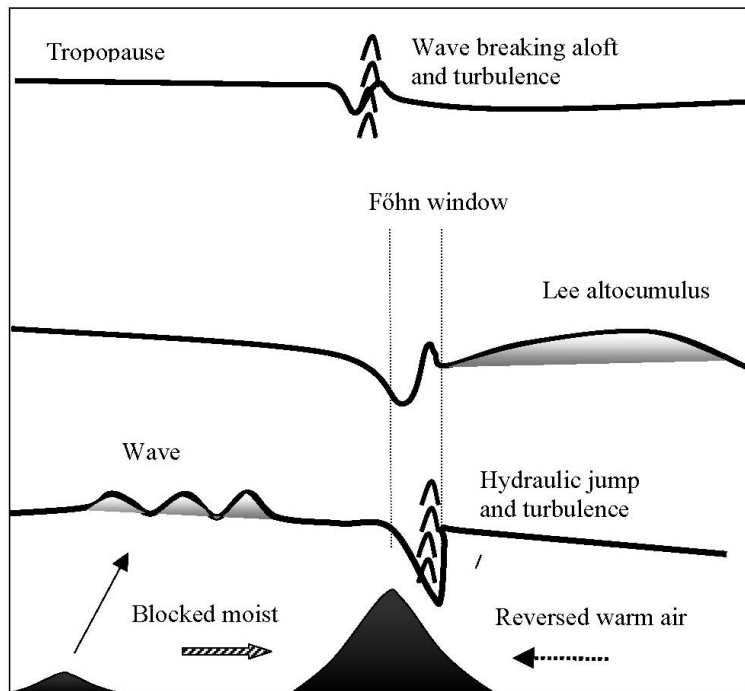


Figure 16. Summary of the relevant dynamical processes during this northerly föhn event.

## 6. CONCLUSION

A northerly föhn event over the Alps is investigated using MAP observational data and COAMPS simulations. The salient characteristics are summarized in Fig. 16. A stable layer is located approximately between 3 and 5 km, below which the cold moist air is blocked to the north of the Alps which have a relatively large non-dimensional mountain height. Evanescent waves excited by low terrain upstream are present to the north of the main Alpine crests. Above the blocked layer, the warmer and dryer air tends to descend while it advects across the Alps. A sudden descent occurs over the lee slope of the main Alpine ridge, associated with enhancement of surface wind speed. Before it reaches the Po valley, the warm air aloft encounters a hydraulic jump, a narrow zone with small Richardson number and large TKE, which helps the air recover its altitude over a short horizontal distance (i.e.  $\sim 10$  km). Below the crest level, the warmer and dryer air (relative to the air to the north of the Alps and at the same level) on the lee side comes from south-east associated with the Sicily cyclone.

COAMPS suggests that the observed altocumulus filaments trailing from the lee of the Alpine ridge are probably irrelevant to hydraulic jumps. More likely, the long cloud filaments are associated with the inertia-gravity wave response, which creates a weak descent-strong ascent-slow descent pattern. The narrow föhn window observed by AVHRR at 0718 UTC is induced by the weak descent, and the long altocumulus downstream is probably associated with the adiabatic cooling corresponding to the sharp ascent and slow descent pattern. The widening of the föhn window corresponds to the large-scale moisture advection rather than the terrain effect.

The blocking and low-level wave breaking have a strong influence on the vertical profile of momentum flux and mountain drag. Momentum deposition occurs at two

different levels—mountain peak level associated with dissipative hydraulic jumps, and wave breaking aloft in the lower stratosphere. Flow stagnation associated with blocking reduces the effective mountain height, and therefore the wave amplitude, and wave drag. As the result, the increase of drag with mountain height is much slower than predicted by linear theory. For high terrain, the non-dimensional effective mountain height is found to be approximately the square root of the real non-dimensional mountain height. This simple empirical formula may be useful in mountain drag parametrizations.

#### ACKNOWLEDGEMENTS

This research was supported by the Office of Naval Research program element 0601153N. The support for the third author was provided by the National Science Foundation, Division of Atmospheric Sciences (ATM-0112354). The data for the field program were collected in a joint effort by the MAP scientists and staff, especially our colleagues in the gravity-wave-breaking team: Drs A. Broad, D. Fritts, K. Hoinka, J. Kuettner, G. Poulos, S. Smith, and H. Volkert. Walters and Morley of NCAR provided the SABL data and Dartiguelongues (Centre National d'Etudes Spatiales) provided CVB data. COAMPS<sup>TM</sup> is a trade mark of the US Naval Research Laboratory.

#### REFERENCES

- Bougeault, P., Binder, P., Buzzi, A., 2001 The MAP special observing period. *Bull. Am. Meteorol. Soc.*, **82**, 433–462
- Dirks, R., Houze, R., Kuettner, J., Smith, R. B., Steinacker, R. and Volkert, H.
- Chen, W. D. and Smith, R. B. 1987 Blocking and deflection of airflow by the Alps. *Mon. Weather Rev.*, **115**, 2578–2597
- Duchon, C. E. 1979 Lanczos filter in one and two dimensions. *J. Applied Meteorol.*, **18**, 1016–1022
- Flamant, C., Richard, E., Schär, C., Rotunno, R., Nance, L., Sprenger, M. and Benoit, R.
- Hafner, T. A. and Smith, R. B. 1985 The wake south of the Alps: Dynamics and structure of the lee-side flow and secondary potential vorticity banners. *Q. J. R. Meteorol. Soc.*, **130**, 1275–1303
- Hodur, R. M. 1997 Pressure drag on the European Alps in relation to synoptic events. *J. Atmos. Sci.*, **21**, 562–572
- The Naval Research Laboratory's Coupled Ocean/Atmosphere Mesoscale Prediction System (COAMPS). *Mon. Weather Rev.*, **125**, 1414–1430
- Hoinka, K. P. 1985 What is Toehn clearance?. *Bull. Am. Meteorol. Soc.*, **66**, 1123–1132
- Huppert, H. E. and Miles, J. M. 1969 Lee waves in a stratified flow: Part 3. Semi-elliptical obstacles. *J. Fluid Mech.*, **35**, 481–496
- Jiang, Q. 2003 Moist dynamics and orographic precipitation. *Tellus*, **55A**, 301–316
- Jiang, Q., Smith, R. B. and Doyle, J. D. 2003 The nature of the Mistral: Observations of modelling of two MAP events. *Q. J. R. Meteorol. Soc.*, **129**, 857–875
- Kim, Y.-J., Eckermann, S. D. and Chun, H.-Y. 2003 An overview of the past, present, and future of gravity-wave drag parameterization for numerical climate and weather prediction models. *Atmos. and Ocean*, **41**, 65–98
- Klemp, J. B. and Lilly, D. K. 1975 The dynamics of wave-induced downslope winds. *J. Atmos. Sci.*, **32**, 320–339
- Lindzen, R. S. 1981 Turbulence and stress owing to gravity wave and tidal breakdown. *J. Geophys. Res.*, **86**, 977–9714
- Mayr, G. J. and McKee, T. B. 1995 Observations of the evolution of orogenic blocking. *Mon. Weather Rev.*, **123**, 1447–1464
- Mellor, G. L. and Yamada, T. 1974 A hierarchy of turbulence closure models for planetary boundary layers. *J. Atmos. Sci.*, **31**, 1791–1806
- Ólafsson, H. and Bougeault, P. 1997 The effect of rotation and surface friction on orographic drag. *J. Atmos. Sci.*, **54**, 193–210
- Pierrehumbert, R. T. and Wyman, B. 1985 Upstream effects of mesoscale mountains. *J. Atmos. Sci.*, **42**, 977–1003

- Queney, P. 1948 The problem of air flow over mountains: A summary of theoretical studies. *Bull. Am. Meteorol. Soc.*, **29**, 16–26
- Schär, C. and Smith, R. B. 1993 Shallow-Water flow past an Isolated topography. Part I: Vorticity production and wake formation. *J. Atmos. Sci.*, **50**, 1373–1400
- Scorer, R. S. 1949 Theory of waves in the lee of mountains. *Q. J. R. Meteorol. Soc.*, **75**, 41–56
- Smith, R. B. 1979 The influence of mountains on the atmosphere. *Adv. Geophys.*, **21**, 87–230
- 1980 Linear theory of stratified hydrostatic flow past an isolated mountain. *Tellus*, **32**, 348–364
- 1985 On severe downslope winds. *J. Atmos. Sci.*, **42**, 2597–2603
- 1989 Mountain-induced stagnation points in hydrostatic flow. *Tellus*, **41A**, 270–274
- Smith, R. B., Skubis, S., Doyle, J. D., Broad, A. S., Kiemle, C. and Volkert, H. 2002 Mountain waves over Mont Blanc: Influence of a stagnant boundary layer. *J. Atmos. Sci.*, **59**, 2073–2092
- Smith, S. A. 2004 Observations and simulations of the 8 November 1999 MAP mountain wave case. *Q. J. R. Meteorol. Soc.*, **130**, 1305–1325